ICASE

A Gas-kinetic Scheme for Multimaterial Flows and Its Application in Chemical Reaction

Yongsheng Lian
The Hong Kong University of Science & Technology, Hong Kong

Kun Xu
The Hong Kong University of Science & Technology, Hong Kong
and
ICASE, Hampton, Virginia

Institute for Computer Applications in Science and Engineering
NASA Langley Research Center
Hampton, VA

Operated by Universities Space Research Association

NASA

July 1999

A GAS-KINETIC SCHEME FOR MULTIMATERIAL FLOWS AND ITS APPLICATION IN CHEMICAL REACTION[*]

YONGSHENG LIAN[†] AND KUN XU[‡]

Abstract. This paper concerns the extension of the multicomponent gas-kinetic BGK-type scheme [26] to multidimensional chemical reactive flow calculations. In the kinetic model, each component satisfies its individual gas-kinetic BGK equation and the equilibrium states of both components are coupled in space and time due to the momentum and energy exchange in the course of particle collisions. At the same time, according to the chemical reaction rule one component can be changed into another component with the release of energy, where the reactant and product could have different γ. Many numerical test cases are included in this paper, which show the robustness and accuracy of kinetic approach in the description of multicomponent reactive flows.

Key words. gas-kinetic method, multicomponent flow, detonation wave

Subject classification. Applied Numerical Methods

1. Introduction. The development of numerical methods for the multimaterial flows have attracted much attention in the past years [15, 22, 8, 9]. One of the main application for these methods is the chemical reactive flow calculations [2, 10, 18]. Research of reactive flows, especially the detonation waves, was pioneered by Zeldovich, von Neumann, and Doering, who developed a well known ZND model. The ZND model consists of a non-reactive shock followed by a reaction zone. Ever since the model was proposed, lots of theoretical and numerical work on this problem have been done. Numerical calculation of the ZND detonation was pioneered by Fickett and Wood [11]. They solved the one-dimensional equations using the method of characteristics in conjunction with a shock fitting method. Longitudinal instability waves were accurately simulated. Later, Taki and Fujiwara applied van Leer's upwind method to calculate two-dimensional traveling detonation waves [23, 24]. They solved the Euler equations coupled with two species equations. The chemical reaction was simulated by a two-step finite-rate model and the transverse instabilities around shock front were clearly observed. It was pointed out by Colella et al in [5] that if the numerical resolution in the detonative shock front is not enough, unphysical solution can be easily generated, such as the wrong shock speed. In order to avoid the unphysical solution, Engquist and Sjögreen [6] obtained a high order TVD/ENO numerical method combined with Runge-Kutta time marching scheme to solve the combustion problem and designed a special treatment in the shock region. Kailasanath et. al [14] extended the Flux-Corrected Transport (FCT) algorithm for detonations. In the early 90s, Bourlioux *et.al.* combined PPM scheme with conservative front tracking and adaptive mesh refinement in the study of detonative waves [2, 3, 4]. They showed the spatial-temporal structure of unstable detonation in one and two spatial dimensions and found good agreement between the numerical simulation and the experimental data. Quirk [21] addressed the particular deficiency of the Godunov type upwind schemes in solving complex flow problems, and suggested

[†]Mathematics Department, The Hong Kong University of Science & Technology, Hong Kong.
[‡]Mathematics Department, The Hong Kong University of Science & Technology, Hong Kong (email: makxu@uxmail.ust.hk); and ICASE, Mail Stop 132C, NASA Langley Research Center, Hampton, VA 23681-2199 (email: kxu@icase.edu).

a hybrid scheme, from which he successfully simulated the galloping in one and two-dimensional detonations. Lindström [18] analyzed the poor convergence of inviscid Euler solutions in the study of detonative waves and suggested to solve the compressible Navier-Stokes equations directly. Most recently, Hwang et al [13] pointed out that not only the resolution of the reaction zone is important, but also the size of the computational domain is critical in the capturing of correct detonative solutions. So far, it is well recognized that a good scheme for the reactive flow must be able to capture correct shock speed, and resolve wave structures in multidimensional case, as well as present the correct period of the possible unsteady oscillation in the wave.

Ever since the gas kinetic scheme was proposed for the compressible flow simulations [25], due to its robustness and accuracy it has attracted more attentions in the CFD community. In this paper, we are going to extend the multicomponent BGK solver [26] to high dimensions, and develop a new scheme with the inclusion of reactive terms. The paper is organized as follows. Section 2 introduces the governing equations for the chemical reactive flows in the 2D case, and describes the numerical method. Section 3 is about the numerical experiments, which include non-reactive shock bubble interaction and ZND wave calculations in both 1D and 2D cases. We also show a new example where the reactant and product could have different γ. Different from previous approach [17], the current method follows the evolution of each species individually, and the scheme is more robust than the previous one.

2. Numerical Method. The focus of this section is to present a kinetic scheme to solve the following reacting compressible Euler equations in the 2-D case,

$$(2.1) \qquad \begin{pmatrix} \rho_1 \\ \rho_2 \\ \rho U \\ \rho V \\ \rho E \end{pmatrix}_t + \begin{pmatrix} \rho_1 U \\ \rho_2 U \\ \rho U^2 + P \\ \rho UV \\ U(\rho E + P) \end{pmatrix}_x + \begin{pmatrix} \rho_1 V \\ \rho_2 V \\ \rho UV \\ \rho V^2 + P \\ V(\rho E + P) \end{pmatrix}_y = \begin{pmatrix} -K(T)\rho_1 \\ K(T)\rho_1 \\ 0 \\ 0 \\ K(T)Q_0\rho_1 \end{pmatrix},$$

where ρ_1 is the density of reactant, ρ_2 is the density of product, $\rho = \rho_1 + \rho_2$ is the total density, ρE is the total energy which include both kinetic and thermal ones, i.e. $\rho E = \frac{1}{2}\rho(U^2 + V^2) + P_1/(\gamma_1 - 1) + P_2/(\gamma_2 - 1)$. Here U, V are the average flow velocities in the x and y directions respectively. Each component has its specific heat ratios γ_1 and γ_2. $P = P_1 + P_2$ is the total pressure, and Q_0 is the amount of heat released per unit mass by reaction. The equation of state can be expressed as $P_1 = \rho_1 RT$ and $P_2 = \rho_2 RT$. $K(T)$ is the chemical reactive rate, which is a function of temperature. The specific form of $K(T)$ will be given in the numerical example section.

The above reactive flow equations will be solved in two steps. In the first step, the nonreactive gas evolution parts are solved using the multimaterial gas-kinetic method. In the second step, the source terms on the right hand side of Eq.(2.1) are included in the update of flow variables inside each cell.

2.1. 2-D Multicomponent BGK Scheme.

2.1.1. Gas-kinetic Governing Equations. The focus of this subsection is to present the multicomponent BGK scheme in two dimensions. For two dimensional problem, the governing equation for the time evolution of each component is the BGK model,

$$(2.2) \qquad \begin{aligned} f_t^{(1)} + u f_x^{(1)} + v f_y^{(1)} &= \frac{g^{(1)} - f^{(1)}}{\tau}, \\ f_t^{(2)} + u f_x^{(2)} + v f_y^{(2)} &= \frac{g^{(2)} - f^{(2)}}{\tau}, \end{aligned}$$

where $f^{(1)}$ and $f^{(2)}$ are particle distribution functions for component 1 and 2 gases, and $g^{(1)}$ and $g^{(2)}$ are the corresponding equilibrium states which $f^{(1)}$ and $f^{(2)}$ approach. The relations between the distribution function and the macroscopic variables are,

$$\int f^{(1)}\phi_\alpha^{(1)}d\Xi^{(1)} + f^{(2)}\phi_\alpha^{(2)}d\Xi^{(2)} = W$$

(2.3)
$$= (\rho_1, \rho_2, \rho U, \rho V, \rho E)^T,$$

where $d\Xi^{(1)} = dudvd\xi_1, d\Xi^{(2)} = dudvd\xi_2,$

$$\phi_\alpha^{(1)} = (1, 0, u, v, \frac{1}{2}(u^2 + v^2 + \xi_1^2))^T$$

$$\phi_\alpha^{(2)} = (0, 1, u, v, \frac{1}{2}(u^2 + v^2 + \xi_2^2))^T,$$

are the moments for individual mass, total momentum, and total energy densities, $\xi_1^2 = \xi_{1,1}^2 + \xi_{1,2}^2 + \cdots + \xi_{1,K_1}^2$ and $\xi_2^2 = \xi_{2,1}^2 + \xi_{2,2}^2 + \cdots + \xi_{2,K_2}^2$. The integration elements are $d\xi_1 = d\xi_{1,1}d\xi_{1,2}...d\xi_{1,K_1}$ and $d\xi_2 = d\xi_{2,1}d\xi_{2,2}...d\xi_{2,K_2}$. K_1 and K_2 are the degrees of the internal variables ξ_1 and ξ_2, which are related to the specific heat ratios γ_1 and γ_2. For the two-dimensional flow, we have

$$K_1 = (5 - 3\gamma_1)/(\gamma_1 - 1) + 1 \qquad \text{and} \qquad K_2 = (5 - 3\gamma_2)/(\gamma_2 - 1) + 1.$$

Instead of individual mass, momentum and energy conservation in a single component flow, for two component gas mixtures the compatibility condition is

(2.4)
$$\int (g^{(1)} - f^{(1)})\phi_\alpha^{(1)}d\Xi^{(1)} + (g^{(2)} - f^{(2)})\phi_\alpha^{(2)}d\Xi^{(2)} = 0, \qquad \alpha = 1, 2, 3, 4, 5.$$

The equilibrium Maxwellian distributions $g^{(1)}$ and $g^{(2)}$ are generally defined as

$$g^{(1)} = \rho_1 \left(\lambda_1/\pi\right)^{\frac{K_1+2}{2}} e^{-\lambda_1((u-U_1)^2+(v-V_1)^2+\xi_1^2)},$$

$$g^{(2)} = \rho_2 \left(\lambda_2/\pi\right)^{\frac{K_2+2}{2}} e^{-\lambda_2((u-U_2)^2+(v-V_2)^2+\xi_2^2)},$$

where λ_1 and λ_2 are function of temperature. Due to the momentum and energy exchange in particle collisions, in most cases, the equilibrium states $g^{(1)}$ and $g^{(2)}$ can be assumed to have the same velocity and temperature at any point in space and time. So, based on given initial macroscopic variables at any point in space and time,

$$W^{(1)} = \int g^{(1)}\phi_\alpha^{(1)}d\Xi^{(1)} = (\rho_1, \rho_1 U_1, \rho_1 V_1, \rho_1 E_1)^T,$$

(2.5)
$$W^{(2)} = \int g^{(2)}\phi_\alpha^{(2)}d\Xi^{(2)} = (\rho_2, \rho_2 U_2, \rho_2 V_2, \rho_2 E_2)^T,$$

we can get the corresponding equilibrium values

$$W^{(1)} = \left(\rho_1, \rho_1 U, \rho_1 V, \frac{1}{2}\rho_1(U^2 + V^2 + \frac{K_1+2}{2\lambda})\right)^T,$$

(2.6)
$$W^{(2)} = \left(\rho_2, \rho_2 U, \rho_2 V, \frac{1}{2}\rho_2(U^2 + V^2 + \frac{K_2+2}{2\lambda})\right)^T,$$

3

where the common values of U, V and λ can be obtained from the conservation requirements,

$$\rho = \rho_1 + \rho_2,$$

$$\rho_1 U_1 + \rho_2 U_2 = \rho U,$$

$$\rho_1 V_1 + \rho_2 V_2 = \rho V,$$

(2.7)
$$\rho_1 E_1 + \rho_2 E_2 = \frac{\rho(U^2 + V^2)}{2} + \frac{(K + 2)\rho}{4\lambda}.$$

With the definition of "averaged" value of internal degree of freedom K,

(2.8)
$$K = \frac{\rho_1 K_1 + \rho_2 K_2}{\rho},$$

and the average γ

(2.9)
$$\gamma = \frac{K + 4}{K + 2},$$

the values U, V and λ can be obtained from Eq.(2.7) explicitly,

(2.10)
$$U = \frac{\rho_1 U_1 + \rho_2 U_2}{\rho},$$

(2.11)
$$V = \frac{\rho_1 V_1 + \rho_2 V_2}{\rho},$$

and

(2.12)
$$\lambda = \frac{1}{4} \frac{(K + 2)\rho}{\rho_1 E_1 + \rho_2 E_2 - \frac{1}{2}\rho(U^2 + V^2)}.$$

As a result, the equilibrium states can be expressed as

(2.13)
$$g^{(1)} = \rho_1 \left(\lambda/\pi\right)^{\frac{K_1 + 2}{2}} e^{-\lambda((u - U)^2 + (v - V)^2 + \xi_1^2)},$$

(2.14)
$$g^{(2)} = \rho_2 \left(\lambda/\pi\right)^{\frac{K_2 + 2}{2}} e^{-\lambda((u - U)^2 + (v - V)^2 + \xi_2^2)}.$$

The governing equations (2.2) basically correspond to viscous multimaterial governing equations, and the scheme presented in the next section is actually solving the Navier-Stokes flow equations, where the dissipative coefficients are proportional to the collision time τ [25].

2.1.2. Multicomponent Gas-kinetic Scheme. Numerically, the Boltzmann equations (2.2) are solved using the splitting method. For example, in the x direction, we solve

$$f_t^{(1)} + u f_x^{(1)} = \frac{g^{(1)} - f^{(1)}}{\tau},$$

$$f_t^{(2)} + u f_x^{(2)} = \frac{g^{(2)} - f^{(2)}}{\tau},$$

and in the y direction,

$$f_t^{(1)} + v f_y^{(1)} = \frac{g^{(1)} - f^{(1)}}{\tau},$$

$$f_t^{(2)} + v f_y^{(2)} = \frac{g^{(2)} - f^{(2)}}{\tau}.$$

In each fractional step, the compatibility condition (2.4) is still satisfied.

For the BGK model, in the x direction the equivalent integral solution of f at a cell interface $x_{i+1/2}$ and time t is

$$f^{(1)}(x_{i+1/2}, t, u, v, \xi_1) = \frac{1}{\tau} \int_0^t g^{(1)}(x', t', u, v, \xi_1) e^{-(t-t')/\tau} dt'$$

(2.15)
$$+ e^{-t/\tau} f_0^{(1)}(x_{i+1/2} - ut)$$

for component 1, and

$$f^{(2)}(x_{i+1/2}, t, u, v, \xi_2) = \frac{1}{\tau} \int_0^t g^{(2)}(x', t', u, v, \xi_2) e^{-(t-t')/\tau} dt'$$

(2.16)
$$+ e^{-t/\tau} f_0^{(2)}(x_{i+1/2} - ut)$$

for component 2, where $x_{i+1/2}$ is the cell interface and $x' = x_{i+1/2} - u(t - t')$ the particle trajectory. There are four unknowns in Eq.(2.15) and Eq.(2.16). Two of them are initial gas distribution functions $f_0^{(1)}$ and $f_0^{(2)}$ at the beginning of each time step $t = 0$, and the others are $g^{(1)}$ and $g^{(2)}$ in both space and time locally around $(x_{i+1/2}, t = 0)$.

Numerically, at the beginning of each time step $t = 0$, we have the macroscopic flow distributions inside each cell i,

$$W_i = (\rho_1, \rho_2, \rho U, \rho V, \rho E)_i^T.$$

From the discretized initial data, we can apply the standard van Leer limiter $L(;)$ to interpolate the conservative variables W_i and get the reconstructed initial data

(2.17)
$$\bar{W}_i(x) = W_i + L(s_{i+}, s_{i-})(x - x_i), \quad \text{for} \quad x \in [x_{i-1/2}, x_{i+1/2}],$$

and $\left(\bar{W}_i(x_{i-1/2}), \bar{W}_i(x_{i+1/2}) \right)$ are the reconstructed point-wise values at the cell interfaces $x_{i-1/2}$ and $x_{i+1/2}$.

In order to simplify the notation, in the following $x_{i+1/2} = 0$ is assumed. With the interpolated macroscopic flow distributions $\bar{W}_i$, the initial distribution functions $f_0^{(1)}$ and $f_0^{(2)}$ in Eq.(2.15) and Eq.(2.16) are constructed as

(2.18)
$$f_0^{(1)} = \begin{cases} \left(1 + a_l^{(1)} x \right) g_l^{(1)}, & x < 0, \\ \left(1 + a_r^{(1)} x \right) g_r^{(1)}, & x > 0, \end{cases}$$

for component 1, and

(2.19)
$$f_0^{(2)} = \begin{cases} \left(1 + a_l^{(2)} x \right) g_l^{(2)}, & x < 0, \\ \left(1 + a_r^{(2)} x \right) g_r^{(2)}, & x > 0, \end{cases}$$

for component 2. The equilibrium states in Eq.(2.15) and Eq.(2.16) around $(x = 0, t = 0)$ are assumed to be

(2.20)
$$g^{(1)} = \left(1 + (1 - H(x)) \bar{a}_l^{(1)} x + H(x) \bar{a}_r^{(1)} x + \bar{A}^{(1)} t \right) g_0^{(1)},$$

and

(2.21)
$$g^{(2)} = \left(1 + (1 - \text{H}(x))\bar{a}_l^{(2)}x + \text{H}(x)\bar{a}_r^{(2)}x + \bar{A}^{(2)}t\right)g_0^{(2)},$$

where $\text{H}(x)$ is the Heaviside function. $g_0^{(1)}$ and $g_0^{(2)}$ are the initial equilibrium states located at the cell interface,

$$g_0^{(1)} = \rho_{1,0}\left(\lambda_0/\pi\right)^{\frac{K_1+2}{2}}e^{-\lambda_0((u-U_0)^2+(v-V_0)^2+\xi_1^2)},$$

(2.22)
$$g_0^{(2)} = \rho_{2,0}\left(\lambda_0/\pi\right)^{\frac{K_2+2}{2}}e^{-\lambda_0((u-U_0)^2+(v-V_0)^2+\xi_2^2)}.$$

The parameters $a_{l,r}^{(1,2)}, \bar{a}_{l,r}^{(1,2)}$ and $\bar{A}^{(1,2)}$ have the forms

$$a_l^{(1,2)} = a_{l,1}^{(1,2)} + a_{l,2}^{(1,2)}u + a_{l,3}^{(1,2)}v + a_{l,4}^{(1,2)}\frac{u^2+v^2+\xi_{1,2}^2}{2},$$

$$a_r^{(1,2)} = a_{r,1}^{(1,2)} + a_{r,2}^{(1,2)}u + a_{r,3}^{(1,2)}v + a_{r,4}^{(1,2)}\frac{u^2+v^2+\xi_{1,2}^2}{2},$$

$$\bar{a}_l^{(1,2)} = \bar{a}_{l,1}^{(1,2)} + \bar{a}_{l,2}^{(1,2)}u + \bar{a}_{l,3}^{(1,2)}v + \bar{a}_{l,4}^{(1,2)}\frac{u^2+v^2+\xi_{1,2}^2}{2},$$

$$\bar{a}_r^{(1,2)} = \bar{a}_{r,1}^{(1,2)} + \bar{a}_{r,2}^{(1,2)}u + \bar{a}_{r,3}^{(1,2)}v + \bar{a}_{r,4}^{(1,2)}\frac{u^2+v^2+\xi_{1,2}^2}{2},$$

$$\bar{A}^{(1,2)} = \bar{A}_1^{(1,2)} + \bar{A}_2^{(1,2)}u + \bar{A}_3^{(1,2)}v + \bar{A}_4^{(1,2)}\frac{u^2+v^2+\xi_{1,2}^2}{2}.$$

All coefficients $a_{l,1}^{(1,2)}, a_{l,2}^{(1,2)}, ..., \bar{A}_4^{(1,2)}$ are local constants. In order to determine all these unknowns, the BGK scheme is summarized as follows.

The equilibrium Maxwellian distribution functions located on the left side of the cell interface $x_{i+1/2}$ for component 1 and 2 are,

$$g_l^{(1)} = \rho_{1,l}\left(\lambda_l/\pi\right)^{\frac{K_1+2}{2}}e^{-\lambda_l((u-U_l)^2+(v-V_l)^2+\xi_1^2)},$$

and

(2.23)
$$g_l^{(2)} = \rho_{2,l}\left(\lambda_l/\pi\right)^{\frac{K_2+2}{2}}e^{-\lambda_l((u-U_l)^2+(v-V_l)^2+\xi_2^2)}.$$

At the location $x = 0$, the relations (2.3) and (2.4) require

$$\bar{W}_i(x_{i+1/2}) \equiv \begin{pmatrix} \bar{\rho}_{1,i} \\ \bar{\rho}_{2,i} \\ (\rho\bar{U})_i \\ (\rho\bar{V})_i \\ (\rho\bar{E})_i \end{pmatrix}_{x_{i+1/2}} = \int g_l^{(1)}\phi_\alpha^1 d\Xi^{(1)} + g_l^{(2)}\phi_\alpha^2 d\Xi^{(2)} = \begin{pmatrix} \rho_{1,l} \\ \rho_{2,l} \\ (\rho U)_l \\ (\rho V)_l \\ (\rho E)_l \end{pmatrix},$$

6

and

$$\bar{W}_{i+1}(x_{i+1/2}) \equiv \begin{pmatrix} \bar{\rho}_{1,i+1} \\ \bar{\rho}_{2,i+1} \\ (\rho\bar{U})_{i+1} \\ (\rho\bar{V})_{i+1} \\ (\rho\bar{E})_{i+1} \end{pmatrix}_{x_{i+1/2}} = \int g_r^{(1)}\phi_\alpha^{(1)}d\Xi^{(1)} + g_r^{(2)}\phi_\alpha^{(2)}d\Xi^{(2)} = \begin{pmatrix} \rho_{1,r} \\ \rho_{2,r} \\ (\rho U)_r \\ (\rho V)_r \\ (\rho E)_r \end{pmatrix},$$

from which we have

$$\begin{pmatrix} \rho_{1,l} \\ \rho_{2,l} \\ U_l \\ V_l \\ \lambda_l \end{pmatrix} = \begin{pmatrix} \bar{\rho}_{1,i} \\ \bar{\rho}_{2,i} \\ \bar{U}_i \\ \bar{V}_i \\ \frac{(K_1+2)\bar{\rho}_{1,i}+(K_2+2)\bar{\rho}_{2,i}}{4\left((\rho\bar{E})_i - \frac{1}{2}\bar{\rho}_i(\bar{U}_i^2+\bar{V}_i^2)\right)} \end{pmatrix}_{x_{i+1/2}}.$$

Similarly,

$$\begin{pmatrix} \rho_{1,r} \\ \rho_{2,r} \\ U_r \\ V_r \\ \lambda_r \end{pmatrix} = \begin{pmatrix} \bar{\rho}_{1,i+1} \\ \bar{\rho}_{2,i+1} \\ \bar{U}_{i+1} \\ \bar{V}_{i+1} \\ \frac{(K_1+2)\bar{\rho}_{1,i+1}+(K_2+2)\bar{\rho}_{2,i+1}}{4\left((\rho\bar{E})_{i+1} - \frac{1}{2}\bar{\rho}_{i+1}(\bar{U}_{i+1}^2+\bar{V}_{i+1}^2)\right)} \end{pmatrix}_{x_{i+1/2}}.$$

Therefore, $g_l^{(1)}$, $g_l^{(2)}$, $g_r^{(1)}$ and $g_r^{(2)}$ are totally determined.

Since $g^{(1)}$ and $g^{(2)}$ have the same temperature and velocity at any point in space and time, as shown in Eq.(2.6), the parameters $(a_{l,1}^{(1,2)}, a_{l,2}^{(1,2)}, a_{l,3}^{(1,2)}, a_{l,4}^{(1,2)})$ are not totally independent. Since $a_{l,2}^{(1,2)}, a_{l,3}^{(1,2)}, a_{l,4}^{(1,2)}$ depend only on derivatives of U_0, V_0 and λ_0, common velocity and temperature in space and time require

$$a_{l,2} \equiv a_{l,2}^{(1)} = a_{l,2}^{(2)}, \qquad a_{l,3} \equiv a_{l,3}^{(1)} = a_{l,3}^{(2)} \qquad \text{and} \qquad a_{l,4} \equiv a_{l,4}^{(1)} = a_{l,4}^{(2)}.$$

This is also true among the parameters $a_{r,2}^{(1)}, a_{r,2}^{(2)}, \ldots, a_{r,2}^{(1)}, a_{r,2}^{(2)}$ on the right hand side of a cell interface. So, inside each cell i, we have

(2.24)
$$\begin{aligned}
\frac{\bar{W}_i(x_{i+1/2}) - \bar{W}_i(x_i)}{x_{i+1/2} - x_i} &\equiv \begin{pmatrix} \omega_1 \\ \omega_2 \\ \omega_3 \\ \omega_4 \\ \omega_5 \end{pmatrix} \\
&= \int \left(a_{l,1}^{(1)} + a_{l,2}u + a_{l,3}v + a_{l,4}\frac{u^2+v^2+\xi_1^2}{2}\right) g_l^{(1)}\phi_\alpha^{(1)}d\Xi^{(1)} \\
&\quad + \left(a_{l,1}^{(2)} + a_{l,2}u + a_{l,3}v + a_{l,4}\frac{u^2+v^2+\xi_2^2}{2}\right) g_l^{(2)}\phi_\alpha^{(2)}d\Xi^{(2)}.
\end{aligned}$$

The above five equations uniquely determine the five unknowns $(a_{l,1}^{(1)}, a_{l,1}^{(2)}, a_{l,2}, a_{l,3}, a_{l,4})$ and the solutions is the following: Define

$$\Pi_1 = \omega_3 - U_l(\omega_1 + \omega_2),$$

$$\Pi_2 = \omega_4 - V_l(\omega_1 + \omega_2),$$

$$\Pi_3 = \omega_5 - \frac{U_l^2 + V_l^2 + \frac{K_1+2}{2\lambda_l}}{2\omega_1} - \frac{U_l^2 + V_l^2 + \frac{K_2+2}{2\lambda_l}}{2\omega_2}.$$

The solutions of Eq.(2.24) are

$$a_{l,4} = \frac{8\lambda_l^2(\Pi_3 - U_l\Pi_1 - V_l\Pi_2)}{(K_1 + 2)\rho_{1,l} + (K_2 + 2)\rho_{2,l}},$$

$$a_{l,3} = \frac{2\lambda_l}{\rho_{1,l} + \rho_{2,l}}\left(\Pi_2 - \frac{(\rho_{1,l} + \rho_{2,l})V_l}{2\lambda_l}a_{l,4}\right),$$

$$a_{l,2} = \frac{2\lambda_l}{\rho_{1,l} + \rho_{2,l}}\left(\Pi_1 - \frac{(\rho_{1,l} + \rho_{2,l})U_l}{2\lambda_l}a_{l,4}\right),$$

$$a_{l,1}^{(2)} = \frac{1}{\rho_{2,l}}\left(\omega_2 - \rho_{2,l}(U_la_{l,2} + V_la_{l,3}) - \rho_2(\frac{U_l^2 + V_l^2}{2} + \frac{K_2 + 2}{4\lambda_l})a_{l,4}\right),$$

$$a_{l,1}^{(1)} = \frac{1}{\rho_{1,l}}\left(\omega_1 - \rho_{1,l}(U_la_{l,2} + V_la_{l,3}) - \rho_1(\frac{U_l^2 + V_l^2}{2} + \frac{K_1 + 2}{4\lambda_l})a_{l,4}\right).$$

With the same method, all terms in $a_r^{(1,2)}$ terms can be obtained.

By taking the limits of $(t \rightarrow 0)$ in Eq.(2.15) and Eq.(2.16), applying the compatibility condition at $(x = x_{i+1/2}, t = 0)$, and using Eq.(2.18, 2.19), we get

$$(\rho_{1,0}, \rho_{2,0}, \rho_0U_0, \rho_0V_0, \rho_0E_0)^T \equiv \int g_0^{(1)}\phi_\alpha^{(1)}\, d\Xi^{(1)} + g_0^{(2)}\phi_\alpha^{(2)}\, d\Xi^{(2)}$$

$$= \lim_{t \to 0} e^{-t/\tau}\int f_0^{(1)}(x_{i+1/2} - ut)\phi^{(1)}\, d\Xi^{(1)} + f_0^{(2)}(x_{i+1/2} - ut)\phi^{(2)}\, d\Xi^{(2)}$$

(2.25) $$= \int\left(\text{H}(u)g_l^{(1)} + (1 - \text{H}(u))g_r^{(1)}\right)\phi_\alpha^{(1)}\, d\Xi^{(1)} + \left(\text{H}(u)g_l^{(2)} + (1 - \text{H}(u))g_r^{(2)}\right)\phi_\alpha^{(2)}\, d\Xi^{(2)}.$$

The right hand side of the above equation can be evaluated explicitly using $g_{l,r}^{(1,2)}$ in Eq.(2.23). Therefore, $\rho_{1,0}$, $\rho_{2,0}$, λ_0, U_0 and V_0 in Eq.(2.22) can be obtained from Eq.(2.25). As a result, $g_0^{(1)}$ and $g_0^{(2)}$ are totally determined. Then, connecting the macroscopic variables

$$W_0 = (\rho_{1,0}, \rho_{2,0}, \rho_0U_0, \rho_0V_0, \rho_0E_0)^T$$

at the cell interface with the cell centered values in Eq.(2.17) on both sides, we obtain the slopes for the macroscopic variables,

$$\frac{W_0 - \bar{W}_i(x_i)}{x_{i+1/2} - x_i}, \quad \text{and} \quad \frac{\bar{W}_{i+1}(x_{i+1}) - W_0}{x_{i+1} - x_{i+1/2}},$$

from which $\bar{a}_l^{(1)}$ and $\bar{a}_l^{(2)}$ in Eq.(2.20) and $\bar{a}_r^{(1)}$ and $\bar{a}_r^{(2)}$ in Eq.(2.21) can be determined using the same techniques for solving Eq.(2.24). At this point, there are only two unknowns $\bar{A}^{(1,2)}$ left for the time evolution parts of the gas distribution functions in Eq.(2.20) and Eq.(2.21).

Substituting Eq.(2.18), Eq.(2.19) and Eq.(2.22) into the integral solutions Eq.(2.15) and Eq.(2.16), we get

$$f^{(1)}(x_{i+1/2}, t, u, v, \xi_1) = (1 - e^{-t/\tau})g_0^{(1)} + \tau(t/\tau - 1 + e^{-t/\tau})\bar{A}^{(1)}g_0^{(1)}$$
$$+ \left(\tau(-1 + e^{-t/\tau}) + te^{-t/\tau}\right)\left(\bar{a}_l^{(1)}\text{H}(u) + \bar{a}_r^{(1)}(1 - \text{H}(u))\right)ug_0^{(1)}$$
$$+ e^{-t/\tau}\left((1 - uta_l^{(1)})\text{H}(u)g_l^{(1)} + (1 - uta_r^{(1)})(1 - \text{H}(u))g_r^{(1)}\right),$$

(2.26)

and

$$f^{(2)}(x_{i+1/2}, t, u, v, \xi_2) = (1 - e^{-t/\tau})g_0^{(2)} + \tau(t/\tau - 1 + e^{-t/\tau})\bar{A}^{(2)}g_0^{(2)}$$

$$+ \left(\tau(-1 + e^{-t/\tau}) + te^{-t/\tau} \right) \left(\bar{a}_l^{(2)} \mathrm{H}[u] + \bar{a}_r^{(2)}(1 - \mathrm{H}(u)) \right) u g_0^{(2)}$$
$$+ e^{-t/\tau} \left((1 - uta_l^{(2)}) \mathrm{H}(u) g_l^{(2)} + (1 - uta_r^{(2)})(1 - \mathrm{H}(u)) g_r^{(2)} \right).$$

(2.27)

In order to evaluate the unknowns $\bar{A}^{(1,2)}$ in the above two equations, we can use the compatibility condition at the cell interface $x_{i+1/2}$ on the whole CFL time step Δt,

$$\int_0^{\Delta t} \int (g^{(1)} - f^{(1)}) \phi_\alpha^{(1)} d\Xi^{(1)} dt + (g^{(2)} - f^{(2)}) \phi_\alpha^{(2)} d\Xi^{(2)} dt = 0,$$

from which we can get

$$\int g_0^{(1)} \bar{A}^{(1)} \phi_\alpha^{(1)} d\Xi^{(1)} + g_0^{(2)} \bar{A}^{(2)} \phi_\alpha^{(2)} d\Xi^{(2)}$$
$$= \int \left(\bar{A}_1^{(1)} + \bar{A}_2 u + \bar{A}_3 v + \bar{A}_4 \frac{u^2 + v^2 + \xi_1^2}{2} \right) g_0^{(1)} \phi_\alpha^{(1)} d\Xi^{(1)}$$
$$+ \left(\bar{A}_1^{(2)} + \bar{A}_2 u + \bar{A}_3 v + \bar{A}_4 \frac{u^2 + v^2 + \xi_2^2}{2} \right) g_0^{(2)} \phi_\alpha^{(2)} d\Xi^{(2)}$$
$$= \frac{1}{\gamma_0} \int \left[\gamma_1 g_0^{(1)} + \gamma_2 u \left(\bar{a}_l^{(1)} \mathrm{H}(u) + \bar{a}_r^{(1)} (1 - \mathrm{H}(u)) \right) g_0^{(1)} \right.$$
$$+ \gamma_3 \left(\mathrm{H}(u) g_l^{(1)} + (1 - \mathrm{H}(u)) g_r^{(1)} \right)$$
$$+ \gamma_4 u \left. \left(a_l^{(1)} \mathrm{H}(u) g_l^{(1)} + a_r^{(1)}(1 - \mathrm{H}(u)) g_r^{(1)} \right) \right] \phi_\alpha^{(1)} d\Xi^{(1)}$$
$$+ \left[\gamma_1 g_0^{(2)} + \gamma_2 u \left(\bar{a}_l^{(2)} \mathrm{H}(u) + \bar{a}_r^{(2)} (1 - \mathrm{H}(u)) \right) g_0^{(2)} \right.$$
$$+ \gamma_3 \left(\mathrm{H}(u) g_l^{(2)} + (1 - \mathrm{H}(u)) g_r^{(2)} \right)$$
$$+ \gamma_4 u \left. \left(a_l^{(2)} \mathrm{H}(u) g_l^{(2)} + a_r^{(2)}(1 - \mathrm{H}(u)) g_r^{(2)} \right) \right] \phi_\alpha^{(2)} d\Xi^{(2)},$$

(2.28)

where

$$\gamma_0 = \Delta t - \tau(1 - e^{-\Delta t/\tau}),$$

$$\gamma_1 = -(1 - e^{-\Delta t/\tau}),$$

$$\gamma_2 = -\Delta t + 2\tau(1 - e^{-\Delta t/\tau}) - \Delta t e^{-\Delta t/\tau},$$

$$\gamma_3 = (1 - e^{-\Delta t/\tau}),$$

and

$$\gamma_4 = -\tau(1 - e^{-\Delta t/\tau}) + \Delta t e^{-\Delta t/\tau}.$$

The right hand side of the Eq.(2.28) is known, therefore all parameters in $\bar{A}^{(1,2)}$ terms can be obtained explicitly.

Finally the time-dependent numerical fluxes for component 1 and component 2 gases across a cell interface can be obtained by taking the moments of the individual gas distribution functions $f^{(1)}$ and $f^{(2)}$ in Eq.(2.15) and Eq.(2.16) separately, which are

$$
\begin{pmatrix} \mathcal{F}_{\rho_1} \\ 0 \\ \mathcal{F}_{\rho_1 U_1} \\ \mathcal{F}_{\rho_1 V_1} \\ \mathcal{F}_{\rho_1 E_1} \end{pmatrix}_{i+1/2} = \int u \phi_\alpha^{(1)} f^{(1)}(x_{i+1/2}, t, u, v, \xi_1) d\Xi^{(1)},
$$

and

$$
\begin{pmatrix} 0 \\ \mathcal{F}_{\rho_2} \\ \mathcal{F}_{\rho_2 U_2} \\ \mathcal{F}_{\rho_2 V_2} \\ \mathcal{F}_{\rho_2 E_2} \end{pmatrix}_{i+1/2} = \int u \phi_\alpha^{(2)} f^{(2)}(x_{i+1/2}, t, u, v, \xi_2) d\Xi^{(2)}.
$$

Integrating the above time-dependent flux functions in a whole time step Δt, we can get the total mass, momentum and energy transports for each component, from which the flow variables in each cell can be updated.

2.2. Reaction Step and Flow Update. After obtaining the flux functions across a cell interface, we need to solve an ODE to account for the source term, i.e. $W_t = S$. More specifically, inside each cell we need to solve

(2.29)
$$
\begin{cases} (\rho_1)_t = -K(T)\rho_1, \\ (\rho_2)_t = K(T)\rho_1, \\ (\rho E)_t = K Q_0 \rho_1. \end{cases}
$$

In the current study, one step forward-Euler method is used to solve the above equations.

In summary, the update of the flow variables inside cell (i,j) from step n to $n+1$ is through the following formulation,

$$
W_{i,j}^{n+1} = W_{i,j}^n - \frac{1}{\Delta V}\left(\Delta y \int_0^{\Delta t}(F_{i-1/2,j} - F_{i+1/2,j})dt + \Delta x \int_0^{\Delta t}(G_{i,j-1/2} - G_{i,j+1/2})dt\right) + \Delta t S_{i,j},
$$

where $S_{i,j}$ is the corresponding source terms in cell (i,j), F and G are numerical fluxes across cell interfaces by solving the multicomponent BGK equations, and ΔV is the area of the cell (i,j).

3. Numerical Examples. In this section, we are going to test the multicomponent BGK scheme for both nonreactive and reactive flow calculations. For the viscous calculations, the collision time τ in the BGK scheme presented in the last section is set to be

$$
\tau = \mu/P,
$$

where μ is the dynamical viscosity coefficient and P is the total local pressure. For the Euler solutions, the collision time in the calculation is defined as

$$
\tau = 0.05\Delta t + \frac{|P_l - P_r|}{P_l + P_r}\Delta t,
$$

where Δt is the CFL time step, and P_l and P_r are the corresponding pressure terms in the states g_l and g_r of the initial gas distribution function f_0. From the above expression, we know that in the smooth region there are about 20 collisions inside each time step in the current inviscid calculations, and the magnitude of corresponding numerical diffusion is about 1/10 of that in the Kinetic Flux Vector Splitting (KFVS) scheme [20, 19, 25]. Also, in comparison with the previous "single component" kinetic method for the reactive flows [17], the current approach is more robust. The detail comparison is shown in [16].

3.1. Nonreactive Multimaterial Flow Calculations. In this subsection, we are going to show two cases about the shock-bubble interactions. The main difference between these two cases is about the initial density difference inside the bubble, which consequently gives different flow pattern around material interface.

CASE(1) A M_s=1.22 shock wave in air hits a Helium cylindrical bubble

We examine the interaction of a $M_s = 1.22$ planar shock wave, moving in the air, with a cylindrical bubble of Helium. Experimental data can be found in [12] and numerical solutions using adaptive mesh refinement has been reported in [22]. Recently, a ghost fluid method has been applied to this case too [8]. A schematic description of computational set-up is shown in Fig.(4.1), where reflection boundary conditions are used on the upper and lower boundaries. The initial flow distribution is determined from the standard shock relation with the given strength of the incident shock wave. The bubble is assumed to be in both thermal and mechanical equilibrium with the surrounding air. The non-dimensionalized initial conditions are,

$$W = (\rho = 1, U = 0, V = 0, P = 1, \gamma = 1.4), \quad \text{pre-shock air}$$
$$W = (\rho = 1.3764, U = -0.394, V = 0, P = 1.5698, \gamma = 1.4), \quad \text{post-shock air}$$
$$W = (\rho = 0.1358, U = 0, V = 0, P = 1, \gamma = 1.67), \quad \text{Helium.}$$

In the computation, the nondimensional cell size used is $\Delta x = \Delta y = 0.25$.

In order to identify weak flow features which are often lost within contour plots, we present a number of Schlieren images. These pictures depict the magnitude of the gradient of the density field,

$$(3.1) \qquad |\Delta\rho| = \sqrt{\left(\frac{\partial\rho}{\partial x}\right)^2 + \left(\frac{\partial\rho}{\partial y}\right)^2},$$

and hence they may be viewed as idealized images; the darker the image the larger the gradient. The density derivatives are computed using straightforward central-differencing. The following nonlinear shading function, ϕ is used to accentuate weak flow features [22],

$$(3.2) \qquad \phi = \exp(-k\frac{|\Delta\rho|}{|\Delta\rho|_{max}}),$$

where k is a constant which takes the value 10 for Helium and 60 for air. For R22 simulation in the next test case, we use 1 for heavy fluid and 80 for air.

Fig.(4.2) shows snapshots of Schlieren-type images at nondimensional time t=0.0 and t=125.0. Before the shock hits the bubble, wiggles usually appear around the bubble because the numerical scheme cannot precisely keep the sharp material interface. The wiggles spread in all directions. When they reach the solid wall, they bounce back. But all these noise have a very small magnitude. After the shock hits the bubble, the original shock wave separates into a reflected and a transmitted shock waves. A complex pattern of discontinuities has formed around the top and bottom of the bubble. Since Helium has a lower

density in comparison with air, any small perturbation at the material interface can easily be amplified to form the instability. This instability at the material interface is closely related to the Richtmyer-Meshkov instability. In comparison with the result in [8], the current scheme could capture the unstable interface structure automatically. The result here is basically consistent with both the experiment and that from the mesh-refinement study [22]. It is an interesting problem to further study shock-bubble interaction case, and understand the dynamics of any special numerical treatment on the interface stability. In our calculations, we do not specifically pick up the location of interfaces.

CASE(2) A M_s=1.22 shock wave hits a R22 cylindrical bubble

With the same scheme, we investigate the interaction of a $M_s = 1.22$ planar shock wave, moving in the air, with a cylindrical bubble of R22. The main difference between this case and the previous one is that the density of the bubble here is much larger than the density of air. The initial data is as follow

$$W = (\rho = 1, U = 0, V = 0, P = 1, \gamma = 1.4), \quad \text{pre-shock air}$$
$$W = (\rho = 1.3764, U = -0.394, V = 0, P = 1.5698, \gamma = 1.4), \quad \text{post-shock air}$$
$$W = (\rho = 3.1538, U = 0, V = 0, P = 1, \gamma = 1.249), \quad \text{R22}.$$

In the numerical experiment we use $\Delta x = \Delta y = 0.25$. Fig.(4.3) shows two snapshots of Schlieren-type images at nondimensional time t=0.0 and t=150.0. Due to the higher density in the bubble region, different from Case (1) the material interface in this case is basically stable. This observation is also consistent with the theoretical understanding and physical experiment.

3.2. Reactive Flow Calculations. The study of detonation wave has been undertaken theoretically and computationally for over a century. The successful theory of Zel'dovich, von Neumann, and Doering has come to be a standard model. The ZND solution for the reacting compressing Euler equations is described in [10], which consists of a non-reactive shook followed by a reaction zone; both the shock and the reaction zone travel at a constant speed D. Given γ and heat release Q_0, there is a minimum shock speed, the so-called Chapman-Jougnet value D_{CJ}, above which the ZND solution can be constructed.

The parameter which relates to the shock speed D of a given detonation wave to the CJ velocity D_{CJ} is the overdrive factor f, which is defined as

$$(3.3) \qquad\qquad f \equiv \left(\frac{D}{D_{CJ}} \right)^2.$$

The value of f determines the stability of the detonative front.

In the following test cases, we only consider the reactive flow with two species, i.e. the reactant and the product. The reactant is converted to the product by a one-step irreversible reactive rule governed by Arrhenius kinetics. The factor $K(T)$, which depends on the temperature, is given by

$$K(T) = K_0 T^\alpha e^{-E^+/T},$$

where K_0 is a positive constant. In the current paper, we assume that $\alpha = 0$ and the gas constant R is normalized to unity. Therefore, the above temperature T is determined by $T = P/\rho$.

One important parameter in the numerical calculation of ZND solution is the half-reaction length $L_{1/2}$, which is defined as the distance for half-completion of the reactant starting from the shock front. Usually the reaction prefactor K_0 is selected such that the half-reaction length is unity. From the Arrhenius formula,

the half reaction length is defined as

$$(3.4) \qquad L_{1/2} = \int_1^{1/2} \frac{D-U}{K_0 Z \exp(\frac{-E^+}{T})} dZ,$$

where D is the speed of the shock, U is the post-shock flow speed.

In the output of numerical results, the mass fraction Z is defined as

$$Z = \frac{\rho_1}{\rho_1 + \rho_2}.$$

Case(1): 1-D stable ZND detonation: $\gamma = 1.2$, $Q_0 = 50$, $E^+ = 50.0$, f = 1.8

This test case is from [2]. The pre-shock state is normalized to $P_0 = \rho_0 = 1$ and velocity $U_0 = V_0 = 0$, the post-shock can be obtained using Chapman-Joguet condition. The prefactor K_0 is chosen to be $K_0 = 145.68913$ so that the length of the half-reaction zone $L_{1/2}$ is unit. This case corresponds to the stable ZND profile. The results with 10, 20 and 40 points/$L_{1/2}$ are shown in Fig.(4.4) and (4.5).

Case(2): 1-D unstable detonation: $\gamma = 1.2, Q_0 = 50, E^+ = 50, f = 1.6$

In order to get a high quality simulation result for the unstable overdriven detonation, a high resolution solution is usually required to resolve the instability. At the same time, the correct capturing of oscillatory period requires a large computational domain. As pointed out in [13], for a particular computation, one can be tempted to keep only a few points behind of the shock, with the reasoning that the information behind the shock either never catches up with, or does not affect the shock during the computation. However, if too small a computational domain behind the shock is specified, the points at the edge of and outside of the computational domain cease to be updated after some time, leading to a corruption of the data in that region. The $U + c$ waves emanating from inappropriate boundary condition eventually catch up with the shock itself, thus erroneously alternate the shock properties. The analysis in [13] shows that if one expects the numerical results at time t to be correct, the computational domain L and t must satisfy the following inequality

$$(3.5) \qquad t < \frac{L}{U + c - D} + \frac{L}{D},$$

where U is the speed of the post-shock flow, and c is the sound speed. For the current test, L should satisfy

$$L \geq 1.88t.$$

This classical unstable detonation wave was first used by Fickett and Wood [11]. An important physical quality for unstable detonation is the pressure history at the precursor shock in the oscillatory ZND wave as a function of time. For a stable ZND wave, this shock pressure history should exhibit small fluctuations about the known precursor shock value and decay as time evolves. In the case of unstable detonations, the shock front pressure history makes larger excursions from the ZND value. For the case with $\gamma = 1.2$, $q_0 = 50$, $E^+ = 50$, and overdrive f = 1.6, according to Erpenbeck [7] this ZND profile is a regular periodic pulsating detonation with maximum shock pressure per period given by 101.1 ± 0.2 while the unperturbed ZND shock pressure is 67.3.

In the current study, the density and pressure are normalized to unit after shock. According to $Q_0 = 50, \gamma = 1.2$, the CJ speed becomes $D_{CJ} = 6.80947$, and the prefactor is chosen to be $K_0 = 230.75$ so as to get unit half-reaction length. The post-shock state can be determined by Chapman-Jouguet condition with the

TABLE 3.1

Maxima and minima pressure vs. time for f=1.6 case and $80/L_{1/2}$.

Time	Maxima	Time	Minimum
7.3513	114.1553	11.8038	60.1576
15.9353	85.0627	18.9221	56.7383
23.3201	98.1318	26.3057	56.7478
30.7833	98.3344	33.6993	56.8976
38.1373	97.8645	41.1103	56.7854
45.6102	98.0387	48.6158	56.5972
53.1075	98.8378	56.0587	56.8738
60.5059	98.1242	63.4607	56.9737
67.9318	97.3600	70.8918	56.6064
75.4233	98.6184	78.3885	56.6841
82.8773	98.7023	85.8014	57.0227
90.2201	97.3901	93.2212	56.7298
97.6928	98.2211		

given shock speed. Due to the "start-up" numerical incompatibility, there is a large initial shock pressure up to 114 at time t equal to 8, see Fig.(4.6). After $t > 15$, the motion of the shock front becomes periodic.

In this test, we observe that at least 20 points/$L_{1/2}$ is needed for getting a correct unstable ZND solution. In Fig.(4.6) and (4.7) we show the numerical results with 20 points/$L_{1/2}$ and 40 points/$L_{1/2}$ respectively. At the same time, the result with 80 points/$L_{1/2}$ is given as a reference. In Table(3.1), the data of local maximum and minimum pressure as a function of time are listed.

Case(3) Weak shock wave hitting the reactant

In order to validate the multicomponent BGK scheme, we design the following 1D case to simulate the chemical reaction in which the reactant and product have different γ. The initial condition is given below,

$$W_L = (\rho_L, U_L, P_L, \gamma_L) = (2.667, 1.479, 4.500, 1.4) \qquad \text{post-shock air}$$
$$W_M = (\rho_M, U_M, P_M, \gamma_M) = (1.0, 0.0, 1.0, 1.4) \qquad \text{pre-shock air}$$
$$W_R = (\rho_R, U_R, P_R, \gamma_R) = (0.287, 0.0, 1.0, 1.2) \qquad \text{(Reactant)}.$$

This case is about a weak shock wave with $M = 2.0$ hitting the reactant. We use the Arrhenius form for the reaction rate with $E^+ = Q_0 = 50$, and $K_0 = 600.0$. The numerical cell size is $\Delta x = 1/2000$. In Fig.(4.8) we show the numerical results at time $t = 0.20$. Since the shock is too weak to construct a ZND solution, the flow motion looks only like a two-component nonreactive gases. From Fig.(4.8), we can see the ordinary incident shock moves faster than that of the transmitted shock, and the weak reflection wave moves backward.

Case(4) Strong shock wave hitting the reactant

We increase the strength of the shock in Case(3) up to $M = 8.0$. The initial condition is given below,

$$W_L = (\rho_L, U_L, P_L, \gamma_L) = (5.565, 7.765, 74.50, 1.4) \qquad \text{post-shock air}$$
$$W_M = (\rho_M, U_M, P_M, \gamma_M) = (1.0, 0.0, 1.0, 1.4) \qquad \text{pre-shock air}$$
$$W_R = (\rho_R, U_R, P_R, \gamma_R) = (0.287, 0.0, 1.0, 1.2) \qquad \text{(Reactant)}.$$

14

In Fig.(4.9) we show the numerical results at time $t = 0.05$. From the figure, we observe that after the shock hits the reactant, a ZND solution is obtained.

Case(5) Viscous Reactive Flow

This case is from [18]. The initial data is a one-dimensional ZND profile in the x-direction. The ZND wave connects the left state $\rho_l = 1.731379$, $U_l = 3.015113$ $V_l = 0$, $\rho_l E_l = 130.4736$ by a Chapman-Jouget detonation with the right state $\rho_r = 1, U_r = 0, V_R = 0, \rho_r E_r = 15$. If no transverse gradient is present in the initial data, the numerical scheme will preserve the one-dimensional ZND profile. So, a periodic perturbation is imposed in the y-direction of the initial ZND profile, where the initial data $W(x, y, 0)$ is set to $W_{ZND}(x + \Delta x \text{NINT}(\frac{0.05}{\Delta x} \cos(4\pi y)))$, where $\text{NINT}(z)$ is the nearest integer to z.

The current test has $Q_0 = E^+ = 50$, $\gamma = 1.2$. The reaction rate K_0 is set to be 10^4. The coefficient of dynamical viscosity μ is set to 1.0e-4. With the above choice of parameters, the half reaction length $L_{1/2}$ of the inviscid one-dimensional Chapman-Jouget detonation wave is equal to 0.0285. In our computation, $\Delta x = \Delta y = \frac{1}{800}$ is used. Therefore, there are about 23 points/$L_{1/2}$.

Based on the analysis in [13], in order to get an accurate solution it is sufficient to use a computational domain $x \in [0, 1.2]$. At the left and the right boundary, we impose the left and right states of the initial traveling wave solution. At the lower and upper boundaries, periodic boundary conditions are used.

Fig.(4.10) shows a sequence of snapshots of the density distributions starting from the time $t = 0.0$. Fig.(4.11) is the snapshot of pressure at later times when the ZND front has a regular periodic oscillating profile. The first picture is taken at $t = \frac{13}{80}$, which is just after the collision of two triple points. This figure clearly shows the formation of a Mach stem. In the next few snapshots, the movement of triple points along the transverse shock front are clearly captured. A high pressure spot develops at the location of triple-point intersection. Fig.(4.12) shows the snapshots of the temperature variations. More figures, such as the mass fraction and vorticity, are presented in [16].

This test case corresponds to the cellular regime [2]. The hot spots in the shock front should display a regular diamond propagating pattern, such as observed in physical experiments. In Fig.(4.13), we plot the numerical soot track of the location of shock front, which is the successive geometric representation of the ZND front profile. Since only the position of the shock front is recorded, one dimensional data is required at each output time. From the numerical soot track display, we can easily observe the formation of cellular pattern.

4. Conclusion. In this paper, we have successfully extended the BGK-type gas-kinetic scheme to multidimensional reactive flows. Since each component of the flow is captured individually, mass conservation is precisely preserved for each component in nonreactive multimaterial flow calculations. For the reactive flow calculations, the mass exchange between different components has been implemented in the current kinetic method, as well as the energy release in the reaction process. Many numerical test cases validate the current approach and show the advantages of the kinetic scheme in the description of multicomponent flow calculations. For example, the unstable and stable material interfaces are captured automatically in the shock-bubble interaction cases.

REFERENCES

[1] P.L. BHATNAGAR, E.P. GROSS, AND M. KROOK, *A Model for Collision Processes in Gases I: Small Amplitude Processes in Charged and Neutral One-component Systems*, Phys. Rev., **94** (1954), pp. 511-525.

[2] A. BOURLIOUX, *Numerical Study of Unsteady Detonations*, Ph.D. Thesis, Princeton University (1991).

[3] A. BOURLIOUX, J. MAJDA, AND V. ROYTBURD, *Theoretical and Numerical Structure for Unstable One-dimensional Detonations*, SIAM J. Appl. Math, **51** (1991), pp. 303-342.

[4] A. BOURLIOUX AND J. MAJDA, *Theoretical and Numerical Structure for Unstable Detonations*, Phil. Trans. R. Soc. Lond. A, **250** (1995), pp. 29-68.

[5] P. COLELLA, A. MAJDA, AND V. ROYTBURD, *Theoretical and Numerical Structure for Reacting Shock Waves*, SIAM J. Sci. and Stat. Comput., **7** (1986), pp. 1059-1080.

[6] S. ENGQUIST AND B. SJÖGREEN, *Robust Difference Approximations of Stiff Inviscid Detonation Waves*, UCLA CAM Report 91-03 (1991).

[7] J.J. ERPENBECK, *Stability of idealized one-reaction detonation*, Phys. Fluids, **7** (1964), pp. 684-696.

[8] R.P. FEDKIW, T. ASLAM, B. MERRIMAN, AND S. OSHER, *A Non-oscillatory Eulerian Approach to Interfaces in Multimaterial Flows (The Ghost Fluid Method)*, J. Comput. Phys., **152** (1999), pp. 457-492.

[9] R.P. FEDKIW, X.D. LIU, AND S. OSHER, *A General Technique for Elimination Spurious Oscillations in Conservative Scheme for Multi-phase and Multi-species Euler Equations*, UCLA CAM Report 97-27 (1997).

[10] W. FICKETT AND W.C. DAVIS, *Detonation*, University of California Press, Berkeley, CA (1979).

[11] W. FICKETT AND W.W. WOOD, *Flow Calculations for Pulsating One-dimensional Detonations*, Physics of Fluids, **9**, No. 3 (1966), pp. 903-916.

[12] J.F. HAAS AND B. STURTEVANT, *Interactions of weak shock waves with cylindrical and spherical gas inhomogeneities*, Journal of Fluid Mechanics, **181** (1987), pp. 41-76.

[13] P. HWANG, R.P. FEDKIW, B. MERRIMAN, A.R. KARAGOZIAN, AND S.J. OSHER, *Numerical Resolution of Pulsating Detonation*, preprint 99-12, UCLA CAM reports (1999).

[14] K. KAILASANATH, E.S. ORAN, J.P. BORIS, AND T.R. YOUNG, *Determination of Detonation Cell Size and the Role of Transverse Waves in Two-dimension Detonations*, Combustion and Flame, **61** (1985), pp. 199-209.

[15] S. KARNI, *Hybrid Multifluid Algorithms*, SIAM J. Sci. Comput, **17** (1997), pp. 1019-1039.

[16] Y.S. Lian, *Two Component Gas-kinetic Scheme for Reactive Flows*, M.Phil Thesis, Hong Kong University of Science and Technology (1999).

[17] Y.S. LIAN AND K. XU, *A Gas-kinetic Scheme for Reactive Flows*, ICASE Report No. 98-55 (1998).

[18] D. LINDSTRÖM, *Numerical Computation of Viscous Detonation Waves in Two Space Dimensions*, Report No. 178 (1996), Department of Computing, Uppsala University.

[19] J.C. MANDAL AND S.M. DESHPANDE, *Kinetic Flux Vector Splitting for Euler Equations*, Computers and Fluids, **23** (1994), pp. 447-478.

[20] D.I. PULLIN, *Direct Simulation Methods for Compressible Inviscid Ideal-gas Flow*, J. of Comput. Phys., **34** (1980), pp. 231.

[21] J.J. QUIRK, *Godunov-type Schemes Applied to Detonation Flows*, ICASE Report No. 93-15 (1993).

[22] J.J. QUIRK AND S. KARNI, *In the dynamics of a shock bubble interaction*, J. Fluid Mech., **318** (1996),

pp. 129.

[23] S. Taki and T. Fujiwara, *Numerical Analysis of Two Dimensional Nonsteady Detonations*, AIAA Journal, **16**, No. 1 (1978).

[24] B. van Leer, *Towards the Ultimate Conservative Difference Scheme IV, A New Approach to Numerical Convection*, J. Comput. Phys., **23** (1977), pp. 276.

[25] K. Xu, *Gas-Kinetic Schemes for Unsteady Compressible Flow Simulations*, von Karman Institute for Fluid Dynamics Lecture Series 1998-03 (1998).

[26] K. Xu, *BGK-based Scheme for Multicomponent Flow Calculations*, J. Comput. Phys., **134** (1997), pp. 122-133.
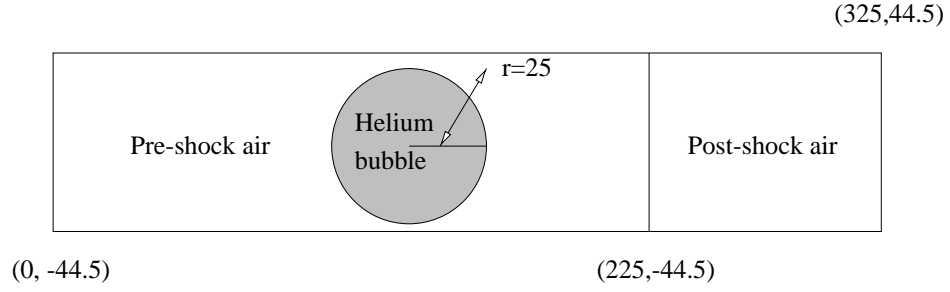
FIG. 4.1. *Physical domain for shock-bubble interaction*
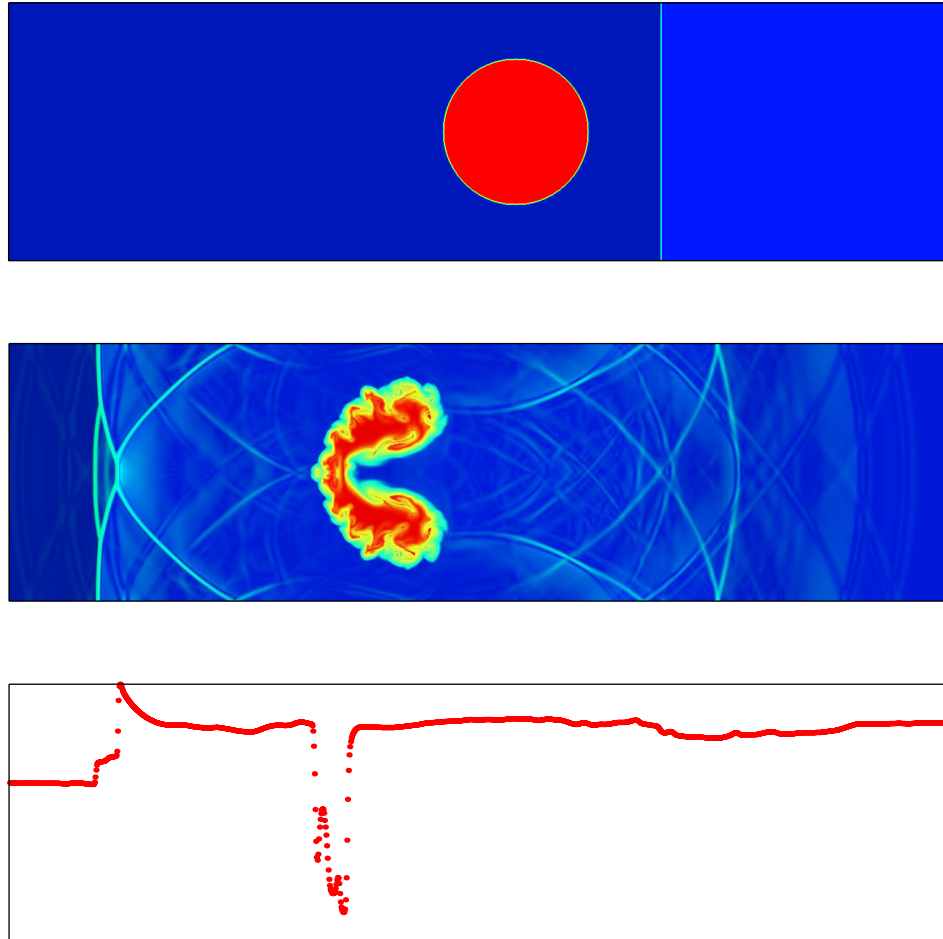
FIG. 4.2. *Numerical Schlieren images of the interaction of an M_s=1.22 shock wave in the air moving from right to left over an Helium cylindrical bubble. The second image is the density distribution at time $t = 125.0$. The third one is the density profile along the centerline of the second figure.*

18
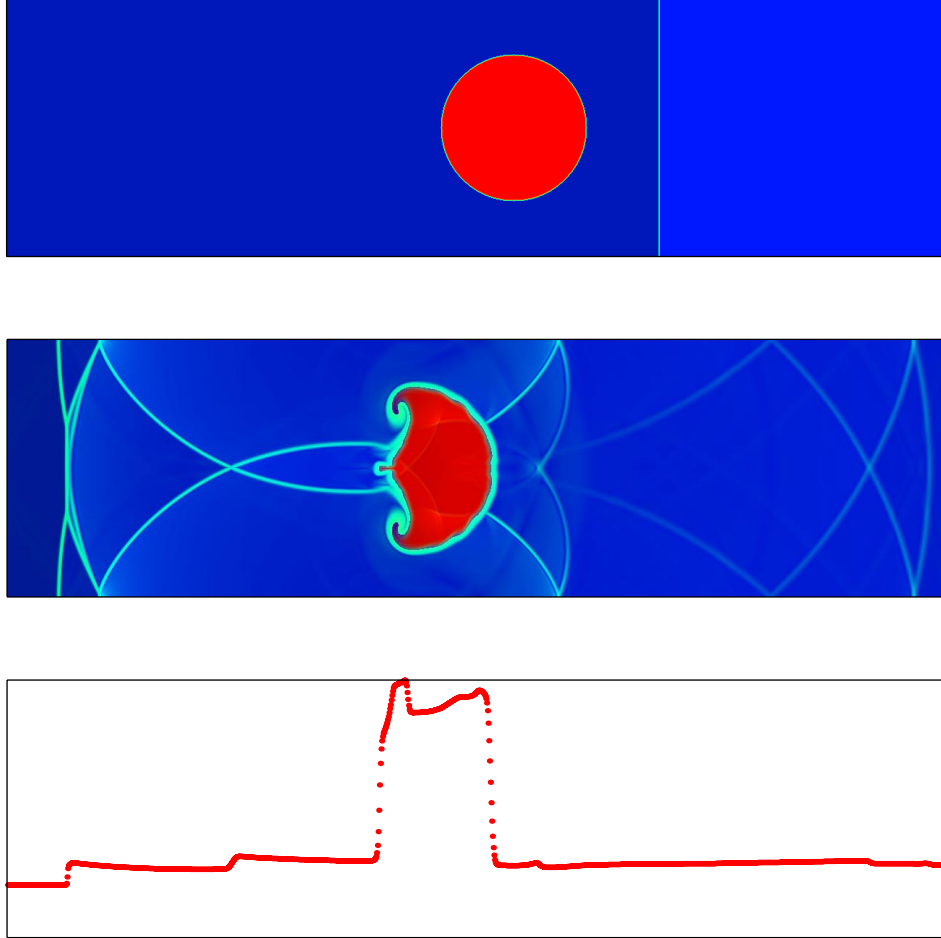
FIG. 4.3. *Numerical Schlieren images of the interaction of an M_s=1.22 shock wave moving from right to left over an R22 cylindrical bubble. The second image is the density distribution at time $t = 150.0$. The thrid one shows the density profile along the centerline of the second figure.*
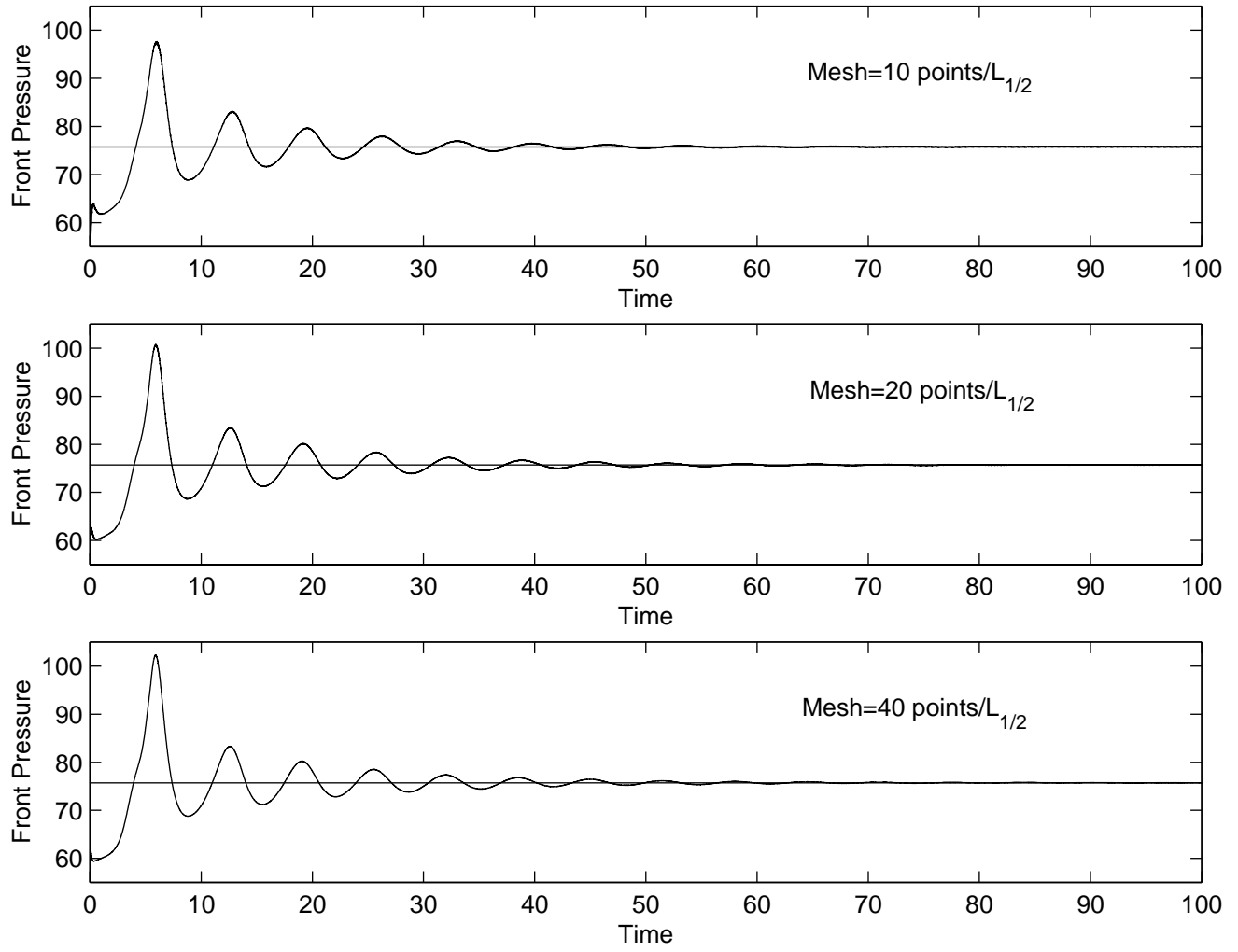
FIG. 4.4. *Mesh refinement study of the pressure history at the shock front for the stable detonation wave, where f=1.8,* $\gamma = 1.2$, $Q_0 = E^+ = 50$, *and* $L_{1/2} = 1.0$ *(CFL=0.5).*
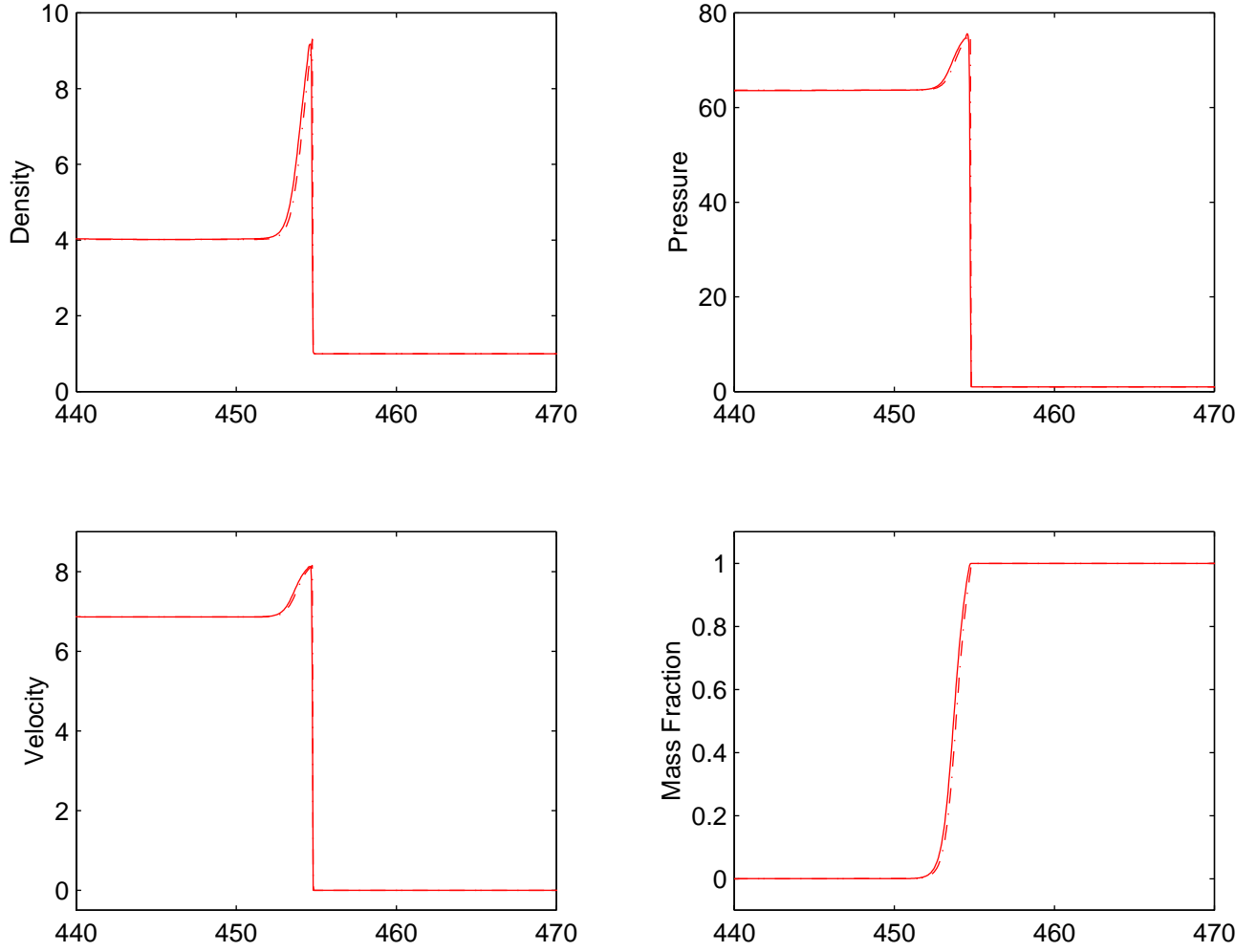
FIG. 4.5. *Numerical solutions (solid line) of density ρ, velocity U, pressure P and mass fraction Z, where f=1.8, $\gamma = 1.2$, $Q_0 = E^+ = 50$, $L_{1/2} = 1.0$, and 10 points/$L_{1/2}$ (CFL=0.5). The dash line is the exact solution.*
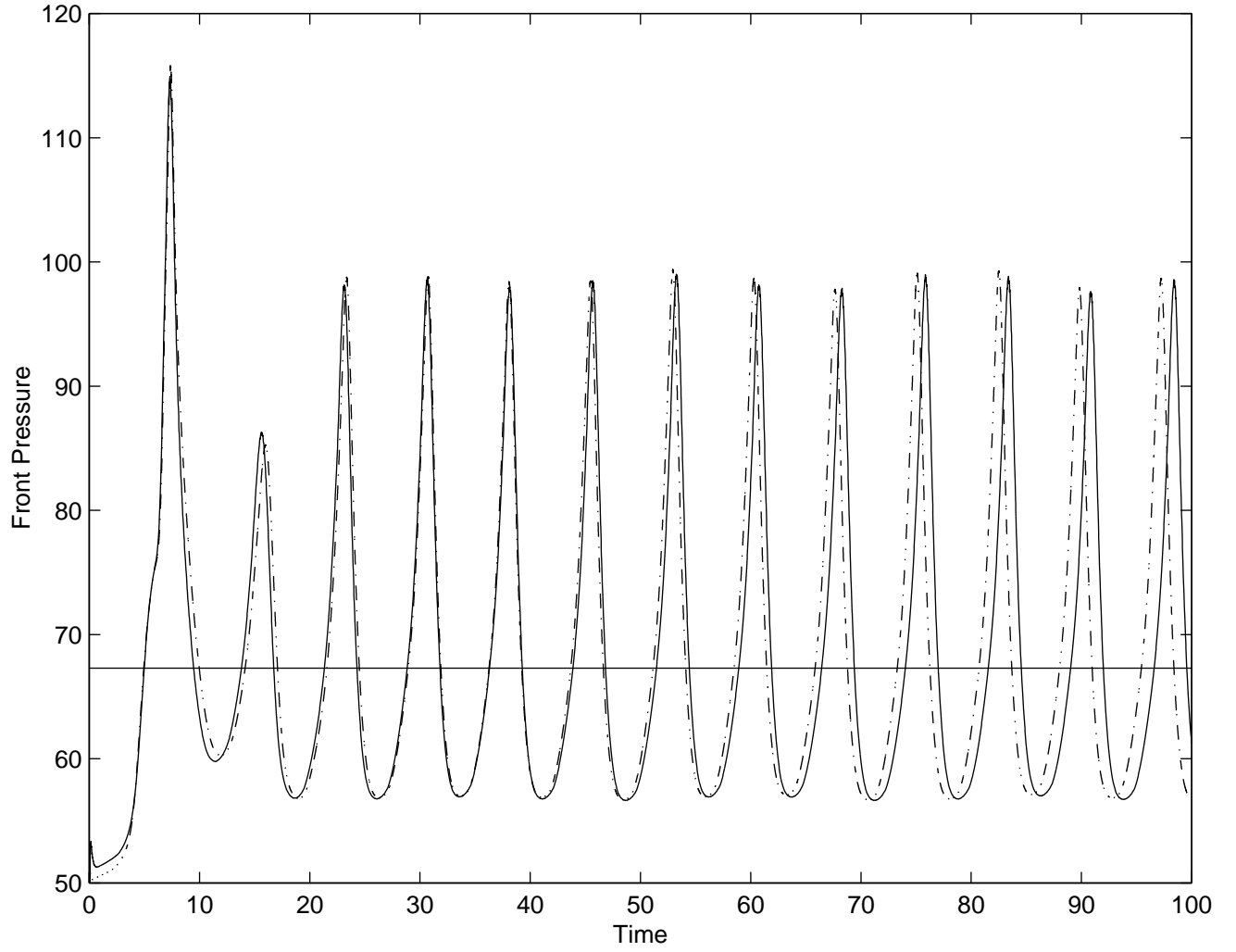
FIG. 4.6. *Local maximum pressure variation as a function of time for the overdriven detonation, where f=1.6, $\gamma = 1.2$, $Q_0 = E^+ = 50$, and $L_{1/2} = 1.0$. Solid line: 80 points/$L_{1/2}$, and dash-dot line: 20 points/$L_{1/2}$ (CFL=0.5) .*
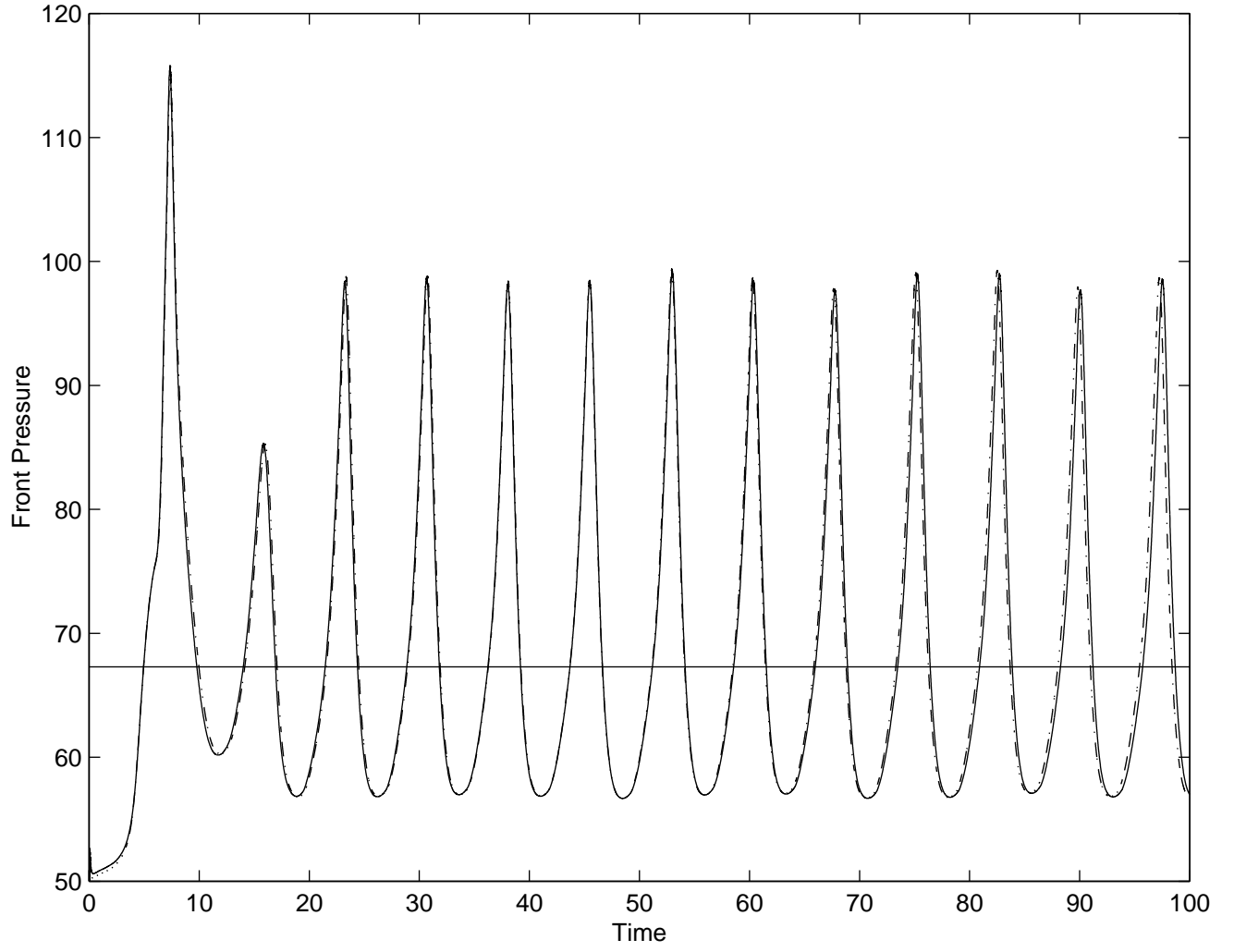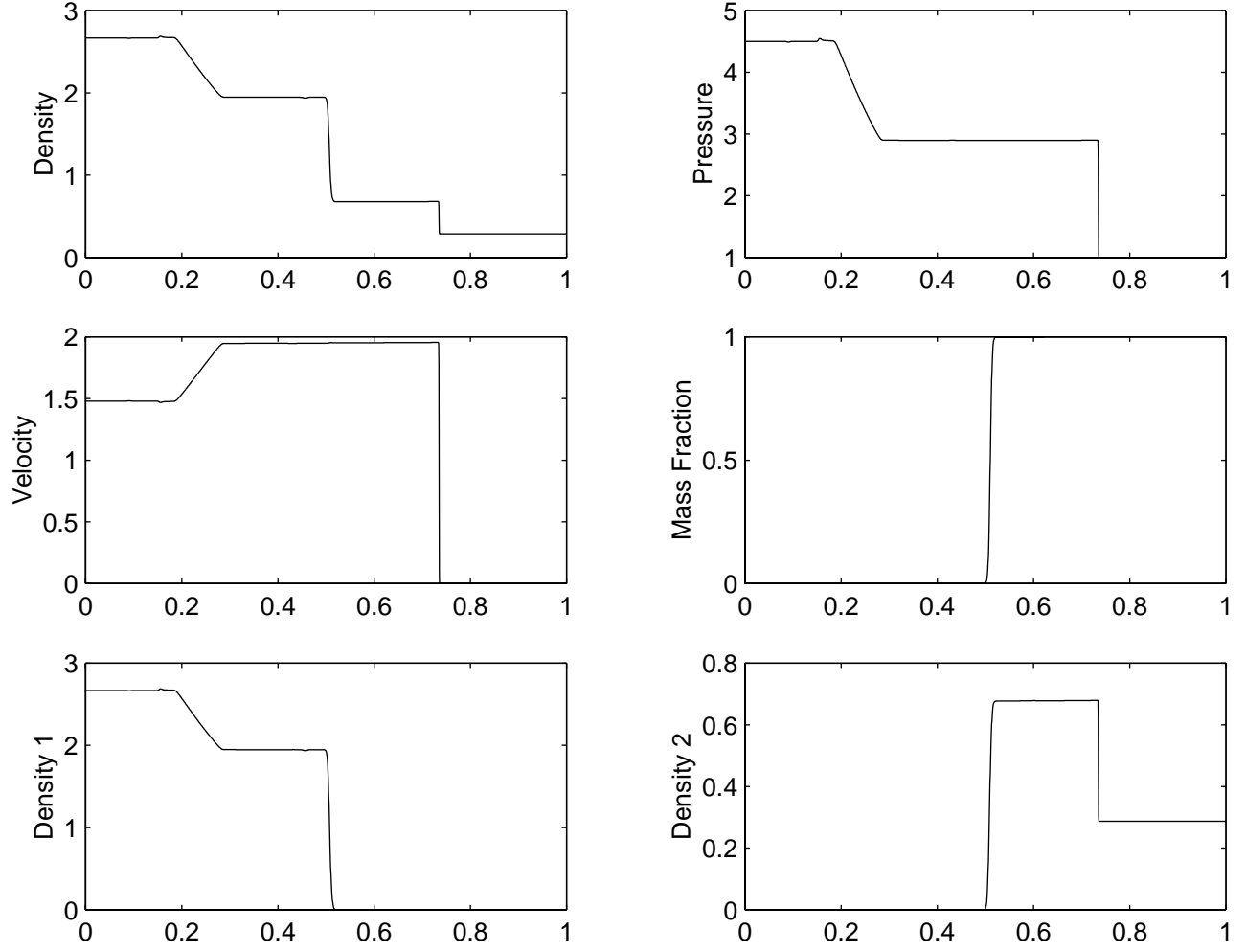
FIG. 4.7. *Local maximum pressure variation as a function of time for the overdriven detonation, where f=1.6, $\gamma = 1.2$, $Q_0 = E^+ = 50$, and $L_{1/2} = 1.0$. Solid line: 80 points/$L_{1/2}$, dash-dot line: 40 points/$L_{1/2}$ (CFL=0.5).*

FIG. 4.8. *Weak shock wave (M = 2.0) in the air (γ = 1.4) hits the reactant gas (γ = 1.2). Δx = 1/2000. The reaction has $E^+ = Q_0 = 50$, and $K_0 = 600.0$ (CFL=0.5).*
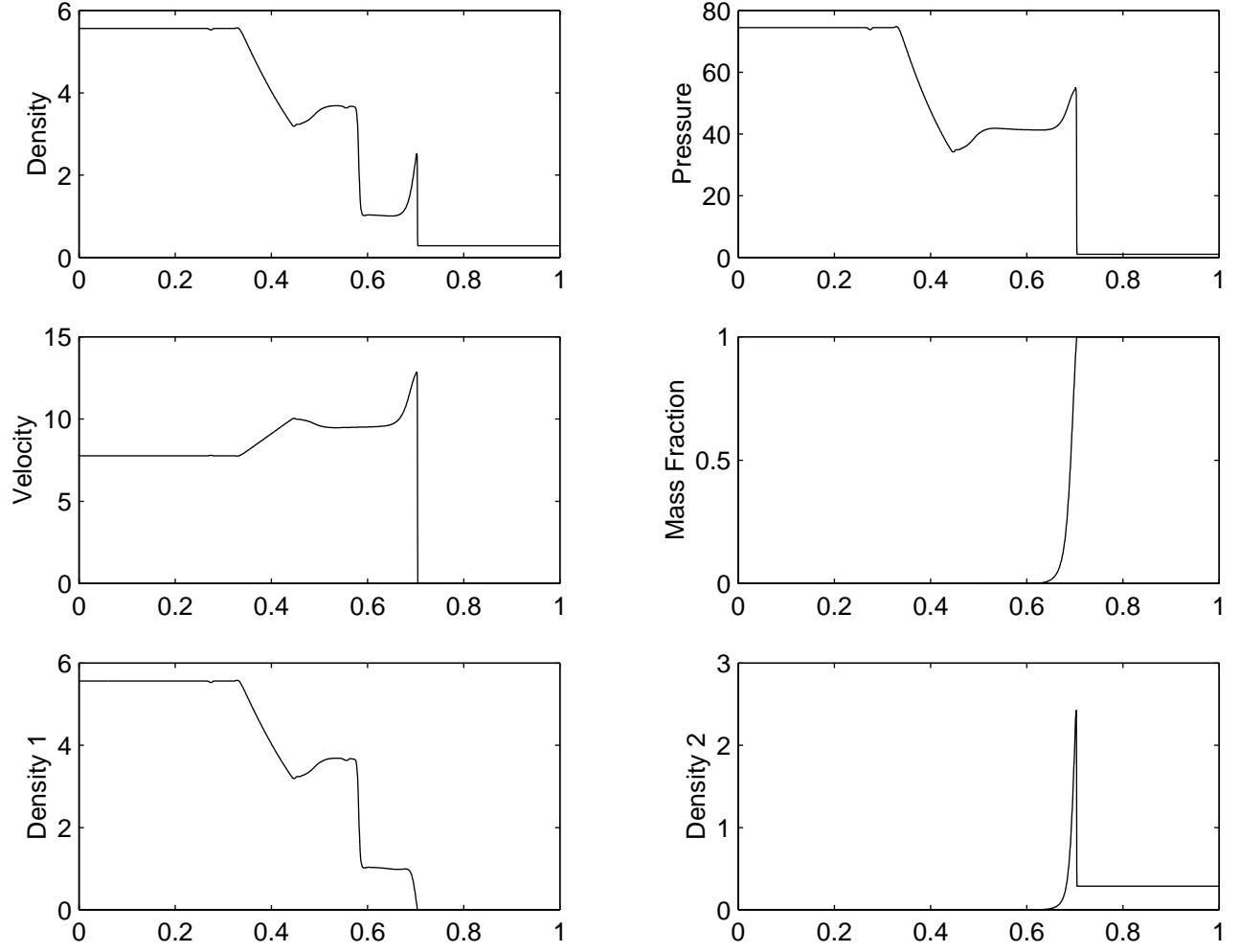
FIG. 4.9. *Strong shock wave (M = 8.00) in the air ($\gamma = 1.4$) hits the reactant gas ($\gamma = 1.2$). $\Delta x = 1/2000$. The reaction has $E^+ = Q_0 = 50.0$, and $K_0 = 600.0$ (CFL=0.5).*
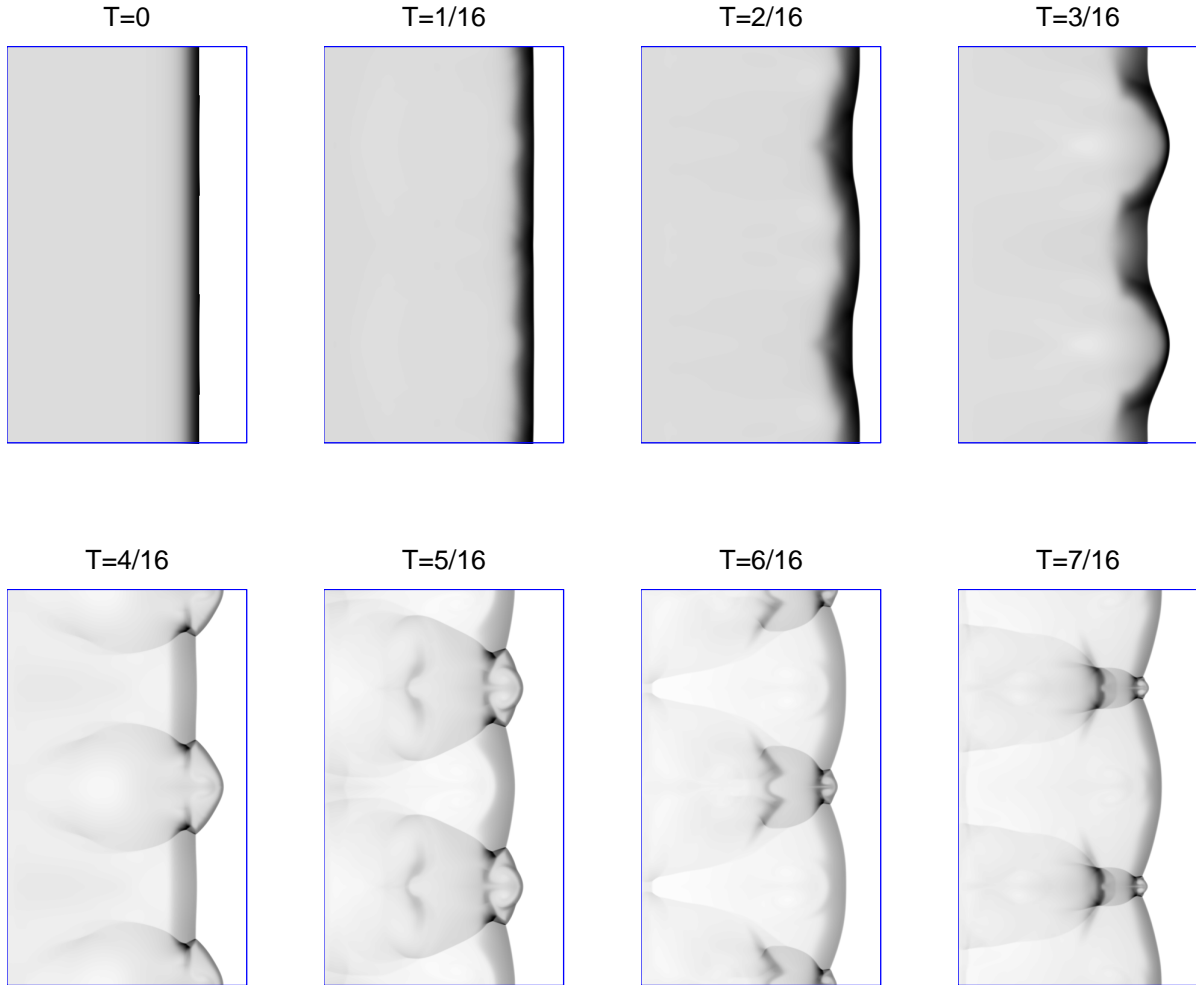
FIG. 4.10. *Sequence of eight snapshots of density starting from time $t = 0$ with the time increment of $\frac{1}{16}$, where $Q_0 = E^+ = 50, \gamma = 1.2$, $\Delta x = \Delta y = \frac{1}{800}$, 23 points/$L_{1/2}$. Shock moves from left to right.*
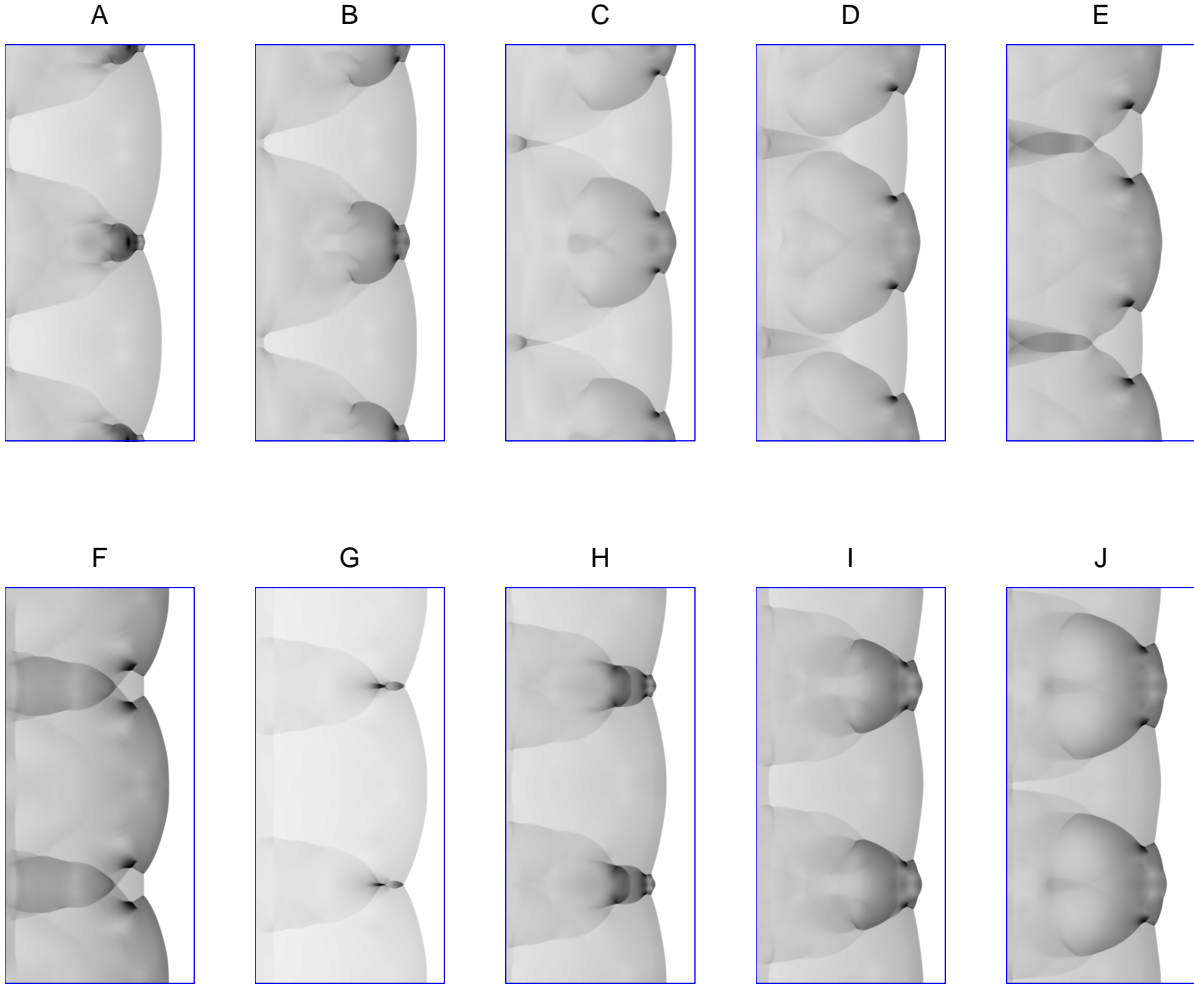
FIG. 4.11. *Sequence of ten snapshots of pressure starting from time $t = \frac{35}{96}$ with each time increment of $\frac{1}{96}$, where $Q_0 = E^+ = 50, \gamma = 1.2, \Delta x = \Delta y = \frac{1}{800}$, 23 points/$L_{1/2}$. Shock moves from left to right.*
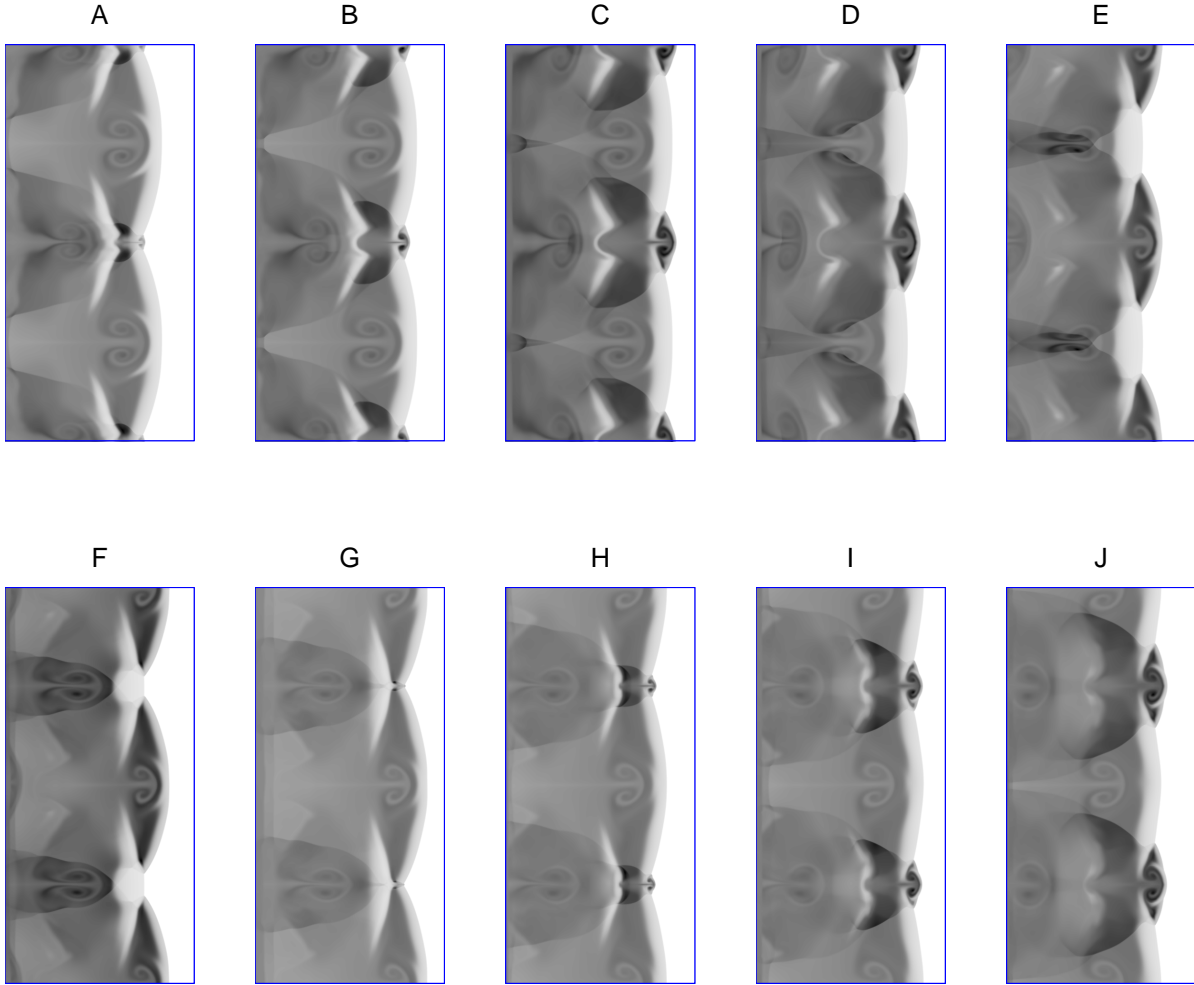
FIG. 4.12. *Sequence of ten snapshots of temperature start from time $t = \frac{35}{96}$ with time increment of $\frac{1}{96}$, where $Q_0 = E^+ = 50, \gamma = 1.2, \Delta x = \Delta y = \frac{1}{800}$, 23 points/$L_{1/2}$. Shock moves from left to right.*
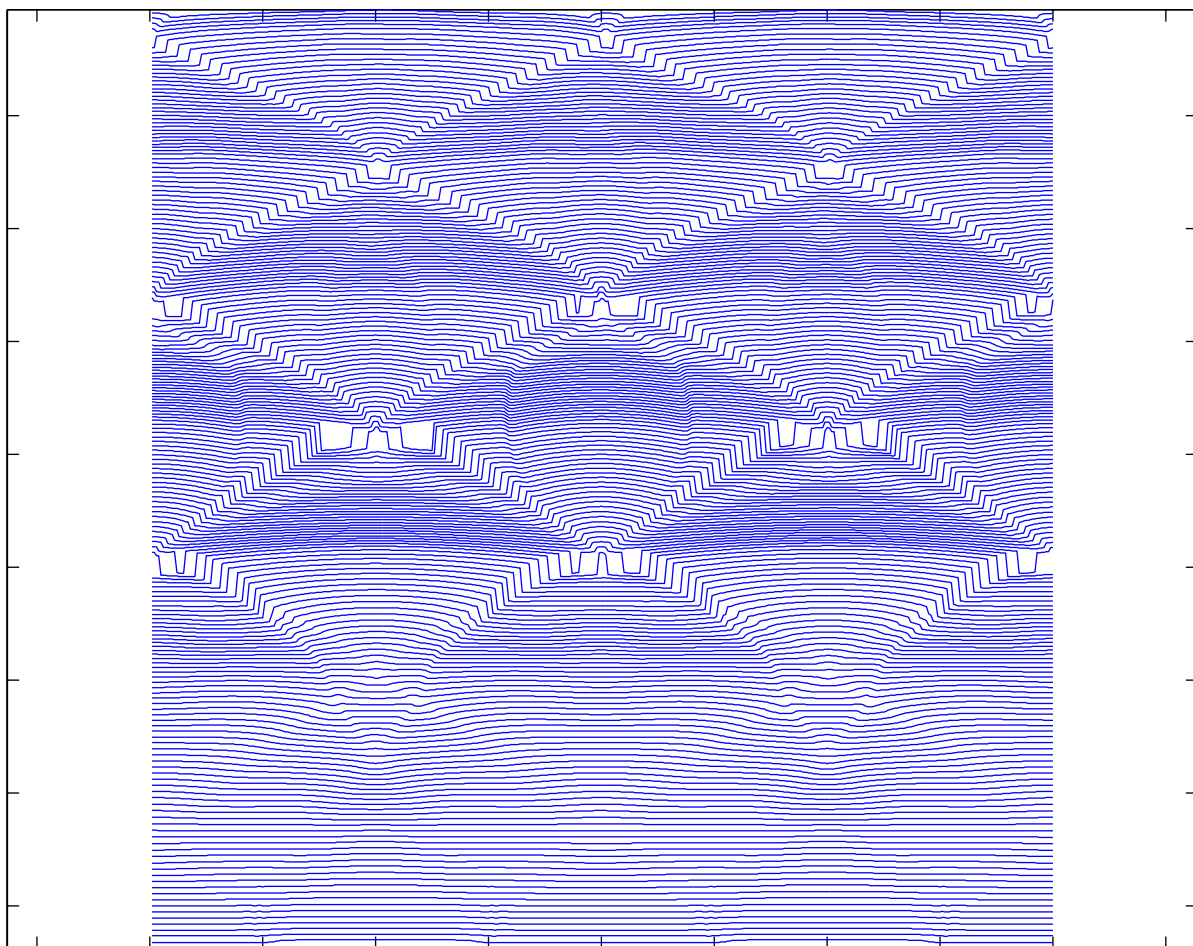
Fig. 4.13. *Numerical soot track: successive geometric representation of the ZND shock front. Each line represents the location of shock front. The vertical axis corresponding to the time.*